



THE UNIVERSITY *of* EDINBURGH

Edinburgh Research Explorer

## A virtual platform of electrical tomography for multiphase flow imaging

**Citation for published version:**

Wang, S, Giorgio-Serchi, F & Yang, Y 2022, 'A virtual platform of electrical tomography for multiphase flow imaging', *Physics of Fluids*, vol. 34, no. 10, 107104. <https://doi.org/10.1063/5.0103187>

**Digital Object Identifier (DOI):**

[10.1063/5.0103187](https://doi.org/10.1063/5.0103187)

**Link:**

[Link to publication record in Edinburgh Research Explorer](#)

**Document Version:**

Publisher's PDF, also known as Version of record

**Published In:**

Physics of Fluids

**General rights**

Copyright for the publications made accessible via the Edinburgh Research Explorer is retained by the author(s) and / or other copyright owners and it is a condition of accessing these publications that users recognise and abide by the legal requirements associated with these rights.

**Take down policy**

The University of Edinburgh has made every reasonable effort to ensure that Edinburgh Research Explorer content complies with UK legislation. If you believe that the public display of this file breaches copyright please contact [openaccess@ed.ac.uk](mailto:openaccess@ed.ac.uk) providing details, and we will remove access to the work immediately and investigate your claim.



# A virtual platform of electrical tomography for multiphase flow imaging

Cite as: Phys. Fluids **34**, 107104 (2022); <https://doi.org/10.1063/5.0103187>

Submitted: 14 June 2022 • Accepted: 07 September 2022 • Accepted Manuscript Online: 09 September 2022 • Published Online: 06 October 2022

Published open access through an agreement with JISC Collections

 Sheng-Nan Wang,  Francesco Giorgio-Serchi and  Yun-Jie Yang



View Online



Export Citation



CrossMark

## ARTICLES YOU MAY BE INTERESTED IN

[Asymmetries and similarities of yawed rotor wakes](#)

Physics of Fluids **34**, 105110 (2022); <https://doi.org/10.1063/5.0106745>

[Structural characteristics of the strong interaction between oblique shock wave and streamwise vortex](#)

Physics of Fluids **34**, 101702 (2022); <https://doi.org/10.1063/5.0121587>

[Photophoresis of spherical particles in slip-flow regime](#)

Physics of Fluids **34**, 103307 (2022); <https://doi.org/10.1063/5.0103646>



Physics of Plasmas   Physics of Fluids  
Special Topic: Turbulence in Plasmas and Fluids  
Submit Today!

# A virtual platform of electrical tomography for multiphase flow imaging

Cite as: Phys. Fluids **34**, 107104 (2022); doi: 10.1063/5.0103187

Submitted: 14 June 2022 · Accepted: 7 September 2022 ·

Published Online: 6 October 2022



View Online



Export Citation



CrossMark

Sheng-Nan Wang,<sup>1,2</sup> Francesco Giorgio-Serchi,<sup>3</sup> and Yun-Jie Yang<sup>1,a)</sup>

## AFFILIATIONS

<sup>1</sup>SMART Group, Institute for Digital Communications, School of Engineering, The University of Edinburgh, EH9 3FG Edinburgh, United Kingdom

<sup>2</sup>College of Electrical, Energy and Power Engineering, Yangzhou University, 225127 Yangzhou, China

<sup>3</sup>Institute for Integrated Micro and Nano Systems, School of Engineering, The University of Edinburgh, EH9 3FG Edinburgh, United Kingdom

<sup>a)</sup> Author to whom correspondence should be addressed: [y.yang@ed.ac.uk](mailto:y.yang@ed.ac.uk)

## ABSTRACT

This paper reports a new approach to quantitatively evaluate the performance of Electrical Tomography (ET) in measuring dynamic multiphase flows. A virtual multiphase flow imaging platform based on ET is constructed and demonstrated on two typical gas–liquid flows, i.e., water–gas flow and oil–gas flow. Two coupling simulation cases, i.e., water–gas flow field and electric currents field coupling simulation and oil–gas flow field and electrostatics field coupling simulation, are performed to simulate multiphase flow sensing of Electrical Impedance Tomography (EIT) and Electrical Capacitance Tomography (ECT). We quantitatively evaluated the representative EIT and ECT image reconstruction algorithms on the virtual evaluation platform bringing evidence of the improved capability to capture the key flow features of the fluid mixture with respect to traditional static phantoms. *Ad-hoc* treatment of the signal noise enables one to better capture dynamic responses of the fluid phase volume fractions and their spatial gradients throughout their mixing along the conduit, ultimately demonstrating unprecedented potential in the quantitative characterization of complex, unsteady multi-phase systems. The proposed image reconstruction constitutes a highly effective platform for quantitative performance evaluation of ET, parameter optimization of model-based ET image reconstruction algorithms, and for the development of data-driven ET algorithms in multiphase flow imaging.

© 2022 Author(s). All article content, except where otherwise noted, is licensed under a Creative Commons Attribution (CC BY) license (<http://creativecommons.org/licenses/by/4.0/>). <https://doi.org/10.1063/5.0103187>

## NOMENCLATURE

$C_{norm}$	Normalized form of capacitances changes
$\mathbf{E}$	Identity matrix
$\mathbf{F}$	Volume force vector
$\mathbf{F}_g$	Gravity force vector
$\mathbf{I}$	Identity tensor
$I(A)$	Amplitude of excitation current
$\mathbf{J}_{ECT}$	Jacobian matrix of ECT
$\mathbf{J}_{EIT}$	Jacobian matrix of EIT
$\mathbf{J}_{norm}$	Normalized form of $\mathbf{J}_{ECT}$
$k$	Iteration number
$\mathbf{L}$	Two-order four connected region Gaussian–Laplace operator matrix
$p$	Pressure
$P[\cdot]$	Truncation operator
$\mathbf{u}$	Velocity vector of the mass averaged mixture

$U(V)$	Amplitude of excitation current
$\alpha$	Iteration step length
$\gamma$	Reinitialization parameter
$\Delta C$	Capacitance variation
$\Delta V$	Induced boundary voltage variation
$\Delta \epsilon$	Permittivity variation
$\Delta \sigma$	Conductivity variation
$\Delta \hat{\sigma}$	Estimated conductivity variation
$\delta$	Interface thickness controlling parameter
$\epsilon$	Permittivity of the gas–liquid medium
$\epsilon_e$	Permittivity of the electrode
$\epsilon_g$	Permittivity of gas
$\epsilon_l$	Permittivity of liquid
$\epsilon_o$	Permittivity of oil
$\epsilon_p$	Permittivity of the pipe
$\epsilon_w$	Permittivity of water
$\epsilon_{norm}$	Normalized permittivity of the gas–liquid medium

$\hat{\epsilon}_{norm}$	The estimated value of $\epsilon_{norm}$
$\epsilon_0$	Vacuum permittivity
$\eta_\theta$	variance of the reconstructed image
$\eta_{\theta\xi}$	Cross-covariance for the reconstructed image and real image
$\eta_\xi$	variance of the real image
$\theta$	Reconstructed image
$\lambda$	Regularization coefficient
$\mu$	Mixture dynamic viscosity
$\mu_g$	Dynamic viscosity of the gas
$\mu_l$	Dynamic viscosity of the liquid
$\mu_o$	Dynamic viscosity of oil
$\mu_w$	Dynamic viscosity of water
$\xi$	real image
$\rho$	Mixture density
$\rho_g$	Density of gas
$\rho_l$	Density of liquid
$\rho_o$	Density of oil
$\rho_w$	Density of water
$\sigma$	Conductivity of the gas–liquid medium
$\sigma_e$	Conductivity of the electrode
$\sigma_g$	Conductivity of gas
$\sigma_l$	Conductivity of liquid
$\sigma_p$	Conductivity of the pipe
$\sigma_w$	Conductivity of water
$\omega$	Angular frequency
$w$	Angular frequency
$\phi$	Gas void fraction
$\varphi$	Electric potential
$\psi_\theta$	Mean intensity of the reconstructed image
$\psi_\xi$	Mean intensity of the real image
AGS	Adaptive Group Sparsity
DOI	Domain of Interest
ECT	Electrical Capacitance Tomography
EIT	Electrical Impedance Tomography
ET	Electrical Tomography
IGLR	Iteration Gaussian–Laplace Regularization
IWFHR	Iterative Weighted Fidelity and Hybrid Regularization
LBP	Linear Back Projection
LI	Projected Landweber Iteration
OES-CS	Oil–gas flow field and Electrostatics field Coupling Simulation
RIE	Relative Image Error
SA-SBL	Structure-Aware Sparse Bayesian Learning
SBL	Sparse Bayesian Learning
SSIM	Structural Similarity Index Measure
STR	Standard Tikhonov Regularization
TR-GL	Tikhonov Regularization based on the Gaussian–Laplace operator
TV	Total variation
WEC-CS	Water–gas flow field and Electric Currents field Coupling Simulation
3D-FECM	Three-dimensional fluid–electric field coupling model

## I. INTRODUCTION

Electrical Tomography (ET), such as Electrical Capacitance Tomography (ECT)<sup>1–3</sup> and Electrical Impedance Tomography (EIT),<sup>4–6</sup>

represents an agile, non-intrusive, and non-radioactive imaging technology. With ET, the time-varying map of electrical properties (e.g., permittivity, conductivity) in the domain of interest (DOI) can be reconstructed to infer the internal profile of the measured object. Promoted by its portability and excellent temporal resolution (up to 1000 frames per second), ET offers unprecedented potential in industrial and biomedical imaging, especially in monitoring dynamic multiphase flows, which are ubiquitous in industrial and biological processes yet prone to limited real-time experimental observation due to the lack of adequate flow visualization and measurement techniques.<sup>7–9</sup> However, existing ET technology suffers from low spatial resolution (around 10% of the sensor diameter) due to its severe ill-posed and nonlinear inverse problems, limiting its use to merely qualitative imaging in most applications.<sup>2,10–13</sup> It has been a long-standing challenge and research focus to improve the image quality of ET.

Persistent efforts in the scientific community have focused on developing advanced image reconstruction algorithms for ET. Iterative optimization methods are commonly used to resolve the nonlinear ill-posed ET inverse problems with regularizations, e.g., Total Variation (TV) regularization,<sup>14</sup> sparse regularization,<sup>15</sup> and sparse representation.<sup>16</sup> Some non-iterative approaches, e.g., Linear Back Projection (LBP),<sup>17</sup> truncated singular value decomposition,<sup>18</sup> and D-bar method,<sup>19</sup> are also widely adopted for real-time ET imaging. The state-of-art ET image reconstruction algorithms, e.g., Sparse Bayesian Learning (SBL),<sup>20</sup> Adaptive Group Sparsity (AGS),<sup>21</sup> model-based deep learning,<sup>22</sup> Iterative Weighted Fidelity and Hybrid Regularization (IWFHR),<sup>23</sup> are reported to acquire high-quality ET images. Despite considerable improvements, the assessment of existing ET reconstruction algorithms for dynamic multiphase flows still remains heavily dependent on static phantom data.<sup>7,24</sup> In addition to the issue of ET inverse problems, the inability to obtain the ground truth of fluid phase distributions (due to the highly random and nonlinear nature of multiphase flows) also hindered the comprehensive assessment of ET image reconstruction algorithms in multiphase flow imaging.<sup>25,26</sup>

Image quality evaluation is essential in optimizing the image reconstruction algorithms of ET.<sup>27,28</sup> Static simulation and phantom-based experimental approaches have been the primary methods for evaluating ET image quality and algorithm performance since the ground truth of dynamic multiphase flow profiles is unavailable in most practical flow facilities. Such static methods have implications for the image reconstruction algorithms' assessment, yet they are oversimplified in many scenarios. Therefore, it is challenging to perform a quantitative evaluation of ET for the dynamic multiphase flow measurement. More realistic configurations call for more advanced evaluation approaches for ET.

To address the issue mentioned above in multiphase flow imaging, Ye *et al.* exploited a fluid–electric field coupling method and reported a two-dimensional simulation coupled model to investigate the image quality of ECT for measuring the dynamic complex two-phase flows.<sup>16,29</sup> Based on the above research studies, we developed a three-dimensional fluid–electric field coupling model (3D-FECM) to dynamically simulate oil–gas two-phase flow imaging and quantitatively evaluated the performance of ECT.<sup>30</sup> Here, we further propose a virtual evaluation platform of ET, expanding the 3D-FECM to two typical ET modalities, i.e., ECT and EIT. Two types of gas–liquid two-phase flows, i.e., the oil–gas flow and the water–gas flow, and virtual ET data, are virtually generated by 3D-FECM and separately used for

ECT and EIT image quality evaluation. We then demonstrate quantitative evaluation results of representative ET image reconstruction algorithms using the virtual platform and commonly adopted metrics.

## II. METHODOLOGY

### A. Principle of 3D-FECM

The 3D-FECM contains a fluid field interface to generate the gas–liquid two-phase flow data and electric field interfaces to model the ET sensors.<sup>30</sup> The dynamic phase distributions and the corresponding electrical measurements from the virtual ET sensors can be simultaneously collected by coupling the fluid and electric fields.

In fluid field simulation, we adopt the laminar two-phase flow interface based on the incompressible Navier–Stokes equations<sup>31</sup> to simulate the gas–liquid flow, which can be expressed as

$$\begin{aligned} \rho \frac{\partial \mathbf{u}}{\partial t} + \rho(\mathbf{u} \cdot \nabla)\mathbf{u} &= \nabla \cdot [-p\mathbf{I} + \mu(\nabla\mathbf{u} + \nabla\mathbf{u}^T)] + \mathbf{F} + \mathbf{F}_g, \quad (1) \\ \nabla \cdot \mathbf{u} &= 0, \quad (2) \end{aligned}$$

where  $\mathbf{u}$  represents the velocity vector of the mass averaged mixture,  $\mathbf{I}$  represents the identity tensor,  $\mathbf{F}$  is the volume force vector,  $\mathbf{F}_g$  is the gravity force vector,  $p$  is the pressure, and  $\mu$  is the mixture dynamic viscosity given by

$$\mu = \mu_l + (\mu_g - \mu_l)\phi. \quad (3)$$

The mixture density  $\rho$  is defined by

$$\rho = \rho_l + (\rho_g - \rho_l)\phi, \quad (4)$$

where  $\mu_l$  and  $\rho_l$  represent the dynamic viscosity and the density of the liquid, respectively;  $\mu_g$  and  $\rho_g$  represent the dynamic viscosity and the density of the gas, respectively; and  $\phi$  is the gas void fraction.

The level set method<sup>32</sup> is used to track the interface between gas and liquid phases, which can be expressed as

$$\frac{\partial \phi}{\partial t} + \mathbf{u} \cdot \nabla \phi = \gamma \nabla \cdot \left( \delta \nabla \phi - \phi(1 - \phi) \frac{\nabla \phi}{|\nabla \phi|} \right), \quad (5)$$

where  $\gamma$  is the reinitialization parameter (set to 1 by default) and  $\delta$  is the interface thickness controlling parameter (set to  $h_{max}/2$ , where  $h_{max}$  is the maximum grid size in the component).

Two electric field interfaces, i.e., the electrostatics interface and the electric currents interface, are used to model the ECT and the EIT sensors, respectively.

In the electric currents interface, the electric potential  $\varphi$  can be determined by the Poisson-type differential equation<sup>33</sup>

$$-\nabla \cdot (\sigma + j\omega\epsilon)\nabla\varphi = 0, \quad (6)$$

where  $\omega$  is the angular frequency and  $\sigma$  and  $\epsilon$  represent the conductivity and the permittivity of the gas–liquid medium, respectively.

In the electrostatics interface, the relationship between  $\varphi$  and  $\epsilon$  can be represented as<sup>29</sup>

$$-\nabla \cdot (\epsilon_0 \epsilon \nabla \varphi) = 0, \quad (7)$$

where  $\epsilon_0$  is the vacuum permittivity.

The equivalent conductivity and permittivity of the mixing fluid can be evaluated by the Wiener Upper Bound formula<sup>34</sup>

$$\sigma = \sigma_g \phi + \sigma_l(1 - \phi), \quad (8)$$

$$\epsilon = \epsilon_g \phi + \epsilon_l(1 - \phi), \quad (9)$$

where  $\sigma_g$  and  $\sigma_l$  represent the electrical conductivity of gas and liquid, respectively, and  $\epsilon_g$  and  $\epsilon_l$  represent the permittivity of gas and liquid, respectively.

### B. Principle of ET

This study employs two ET modalities for imaging performance evaluation, i.e., EIT and ECT.

#### 1. Electrical impedance tomography

By exploiting the time-difference imaging of EIT, the induced boundary voltage changes ( $\Delta\mathbf{V}$ ) can be measured to reconstruct the conductivity variation in DOI ( $\Delta\sigma$ ). The relationship between  $\Delta\mathbf{V}$  and  $\Delta\sigma$  can be simplified to a linearized model,<sup>35</sup>

$$\Delta\mathbf{V} = \mathbf{J}_{EIT}(\Delta\sigma), \quad (10)$$

where  $\mathbf{J}_{EIT}$  is a Jacobian matrix, i.e., the sensitivity distribution of the EIT sensor.

Image reconstruction of EIT is a typical ill-posed inverse problem, which can be solved by applying the following optimization framework,

$$\Delta\hat{\sigma} = \arg \min_{\Delta\sigma} d(\Delta\mathbf{V}, \mathbf{J}_{EIT}\Delta\sigma) + \lambda R(\Delta\sigma), \quad (11)$$

where  $\Delta\hat{\sigma}$  is the estimated conductivity variation,  $\lambda$  denotes the regularization coefficient,  $d(\Delta\mathbf{V}, \mathbf{J}_{EIT}\Delta\sigma)$  is the data-fidelity term, and  $R(\Delta\sigma)$  represents the regularization term that encodes the prior information of the conductivity variation.

Standard Tikhonov Regularization (STR)<sup>36</sup> is the most standard regularization algorithm in EIT image reconstruction, which is expressed as

$$\Delta\hat{\sigma} = \arg \min_{\Delta\sigma} \frac{1}{2} (\|\Delta\mathbf{V} - \mathbf{J}_{EIT}\Delta\sigma\|^2 + \|\lambda\mathbf{E}\Delta\sigma\|^2), \quad (12)$$

where  $\mathbf{E}$  denotes the identity matrix, which can be substituted by the Gaussian–Laplace operator to penalize the fringe effect in image reconstruction. The Tikhonov regularization based on the Gaussian–Laplace operator<sup>37</sup> is given by

$$\Delta\hat{\sigma} = \arg \min_{\Delta\sigma} \frac{1}{2} (\|\Delta\mathbf{V} - \mathbf{J}_{EIT}\Delta\sigma\|^2 + \|\lambda\mathbf{L}\Delta\sigma\|^2), \quad (13)$$

where  $\mathbf{L}$  denotes the two-order four connected region Gaussian–Laplace operator matrix.

Iterative methods are usually adopted in EIT image reconstruction to improve image quality. The iteration form of (13), named Iteration Gaussian–Laplace Regularization (IGLR),<sup>37</sup> is expressed as

$$\Delta\hat{\sigma}^{(k+1)} = \Delta\hat{\sigma}^{(k)} - \alpha \left[ \mathbf{J}_{EIT}^T (\mathbf{J}_{EIT}\Delta\hat{\sigma}^{(k)} - \Delta\mathbf{V}) + \lambda\mathbf{L}^T\mathbf{L}\Delta\hat{\sigma}^{(k)} \right], \quad (14)$$

where  $k$  is the iteration number,  $\Delta\hat{\sigma}^{(k)}$  is the estimated conductivity variation at the  $k$ th iteration, and  $\alpha$  is the iteration step length.

We also introduce the state-of-the-art Structure-Aware Sparse Bayesian Learning (SA-SBL)<sup>20</sup> for EIT imaging performance

evaluation. From a Bayesian perspective, the optimization problem in (11) can ultimately be formulated as

$$\Delta \hat{\sigma} = \arg \min_{\Delta \sigma} -\log p(\Delta \mathbf{V} | \Delta \sigma) - \lambda \log p(\Delta \sigma), \quad (15)$$

where the log-likelihood term  $\log p(\Delta \mathbf{V} | \Delta \sigma)$  enforces data fidelity; the parametric log-prior term  $\lambda \log p(\Delta \sigma)$  embodies structural constraints that reflect the prior knowledge.

## 2. Electrical capacitance tomography

ECT estimates the permittivity distribution in DOI through inter-electrode capacitance measurements, where the change of capacitances ( $\Delta C$ ) in response to the permittivity variation ( $\Delta \epsilon$ ) can be approximated by<sup>3</sup>

$$\Delta C = \mathbf{J}_{ECT}(\Delta \epsilon), \quad (16)$$

where  $\mathbf{J}_{ECT}$  is the Jacobian matrix, i.e., the sensitivity distribution of the ECT sensor.

A normalized form of Eq. (16) can be written as

$$\mathbf{C}_{norm} = \mathbf{J}_{norm} \epsilon_{norm}, \quad (17)$$

where  $\mathbf{C}_{norm}$  and  $\mathbf{J}_{norm}$  are the normalized form of  $\Delta C$  and  $\mathbf{J}_{ECT}$ , respectively, and  $\epsilon_{norm}$  represents the normalized permittivity.

The image reconstruction of ECT is to determine  $\epsilon_{norm}$  based on  $\mathbf{C}_{norm}$  and  $\mathbf{J}_{norm}$ . Linear Back Projection (LBP) is the most reference algorithm in ECT image reconstruction and is widely used for real-time imaging due to its simplicity and fast speed. By using LBP, the estimated value of normalized permittivity distribution ( $\hat{\epsilon}_{norm}$ ) can be calculated,<sup>3</sup>

$$\hat{\epsilon}_{norm} = \mathbf{J}_{norm}^T \mathbf{C}_{norm}. \quad (18)$$

Projected Landweber Iteration (LI)<sup>38</sup> is one of the most commonly used iterative algorithms for ECT, which can be expressed as

$$\hat{\epsilon}_{norm}^{(k+1)} = P \left[ \hat{\epsilon}_{norm}^{(k)} - \alpha \mathbf{J}_{norm}^T (\mathbf{J}_{norm} \hat{\epsilon}_{norm}^{(k)} - \mathbf{C}_{norm}) \right], \quad (19)$$

$$P[f(\cdot)] = \begin{cases} 0 & \text{if } f(\cdot) < 0, \\ f(\cdot) & \text{if } 0 \leq f(\cdot) \leq 1, \\ 1 & \text{if } f(\cdot) > 1, \end{cases} \quad (20)$$

where  $k$  is the iteration number,  $\hat{\epsilon}_{norm}^{(k)}$  is the estimated normalized permittivity distribution at the  $k$ th iteration,  $\alpha$  is the iteration step length, and  $P[\cdot]$  is a truncation operator.

The Tikhonov method is a universal regularization tool to solve ECT inverse problems. In ECT image reconstruction, the Tikhonov regularization based on the Gaussian–Laplace operator (TR–GL)<sup>37</sup> can be expressed as

$$\hat{\epsilon}_{norm} = (\mathbf{J}_{norm}^T \mathbf{J}_{norm} + \lambda \mathbf{L}^T \mathbf{L})^{-1} \mathbf{J}_{norm}^T \mathbf{C}_{norm}, \quad (21)$$

where  $\lambda$  is the regularization coefficient and  $\mathbf{L}$  is the two-order four connected region Gaussian–Laplace operator matrix.

## III. THREE-DIMENSIONAL FLUID-ELECTRIC FIELD COUPLING SIMULATION

Figure 1 shows a pilot-scale multiphase flow facility at the Multiphase Flow Engineering Laboratory of the Tsinghua International Graduate School, which mainly consists of a gas storage

tank, a multiphase flow separator, gas, and liquid single-phase flow sections, the mixing section, and the control system. The testing section of the facility has an internal diameter of 50 mm, in which a 12-electrode ECT sensor with a transparent window is installed for visual observation. We developed a 3D-FECM to duplicate the testing section of the multiphase flow facility. In the facility, single-phase flows of gas and liquid are separately supplied and controlled to generate gas–liquid flows with different volumetric concentrations. Similarly, in 3D-FECM, dynamic flows of gas and liquid are separately regulated to simulate various gas–liquid flows.

### A. Validation experiment

Validation experiments were undertaken to assess the performance of 3D-FECM. During the experiment, the working gas and liquid are air (permittivity 1.0, density 1.3 kg/m<sup>3</sup>) and white oil (permittivity 2.18, density 879 kg/m<sup>3</sup>), respectively. The working pressure in the testing section is set to 0.6 MPa, and the experimental temperature is about 30 °C. Three working conditions, labeled as case 1, case 2, and case 3, are set for comparison: Case1 is the initial working condition where the pipe in the testing section is filled with oil; in case 2, the volume flow rate of air and white oil is set as 20.0 and 5.0 m<sup>3</sup>/h, respectively; and in case 3, the volume flow rate of air and white oil is set as 100.0 and 2.5 m<sup>3</sup>/h, respectively.

In line with the experimental setup, we conducted a 3D field coupling simulation using COMSOL Multiphysics and Matlab. The gas phase for gas–liquid flow simulation is set as air with permittivity  $\epsilon_g = 1.0$ , density  $\rho_g = 1.3 \text{ kg/m}^3$ , and dynamic viscosity  $\mu_g = 1.81 \times 10^{-5} \text{ Pa}\cdot\text{s}$ . The liquid phase is set as white oil with permittivity  $\epsilon_o = 2.18$ , density  $\rho_o = 879 \text{ kg/m}^3$ , and dynamic viscosity  $\mu_o = 0.02 \text{ Pa}\cdot\text{s}$ . To optimize the computational efficiency of the coupling simulation, we constrain the operational conditions to isothermal by prescribing the temperature of the system to a constant value of 303.15 K, thus configuring the gas–liquid flow as incompressible, and the physical and chemical properties of each phase to be independent of the pressure. We imposed the inlet velocity and outlet pressure boundary conditions to avoid convergence issues in the gas–liquid two-phase flow simulation. We prescribe backflow suppression at the outlet boundary to prevent recirculation and the wall boundary condition as no-slip. Gas–liquid flows with different volumetric concentrations were generated by regulating inlet gas and liquid velocities perpendicular to the entrance surfaces.

Figures 2(a) and 2(b) shows examples of typical gas–liquid flows generated from the experimental flow facility and the 3D-FECM, respectively. Liquid Volume Fraction (LVF) is taken here as the key validation parameter describing the gas–liquid flow system.<sup>39</sup> During the experiments, we first applied ECT to continuously measure the gas–liquid flow by LBP when the experimental condition is in a quasi-static state, then adopted the image-based method to calculate LVF. By averaging the continuous measurements, the mean value of LVF for each working condition can be obtained. Figure 3 shows the comparisons of the LVF results between the simulation and experiment. It can be seen that, as working condition changes, the change of simulation results is in accordance with that of the experimental results. While this provides confidence in the capability to capture the baseline flow features, discrepancies between simulation and experiment are apparent. Despite the established background in fundamental multiphase flow, accurate modeling of more complex and highly unsteady systems remains an extremely challenging field of very active investigation

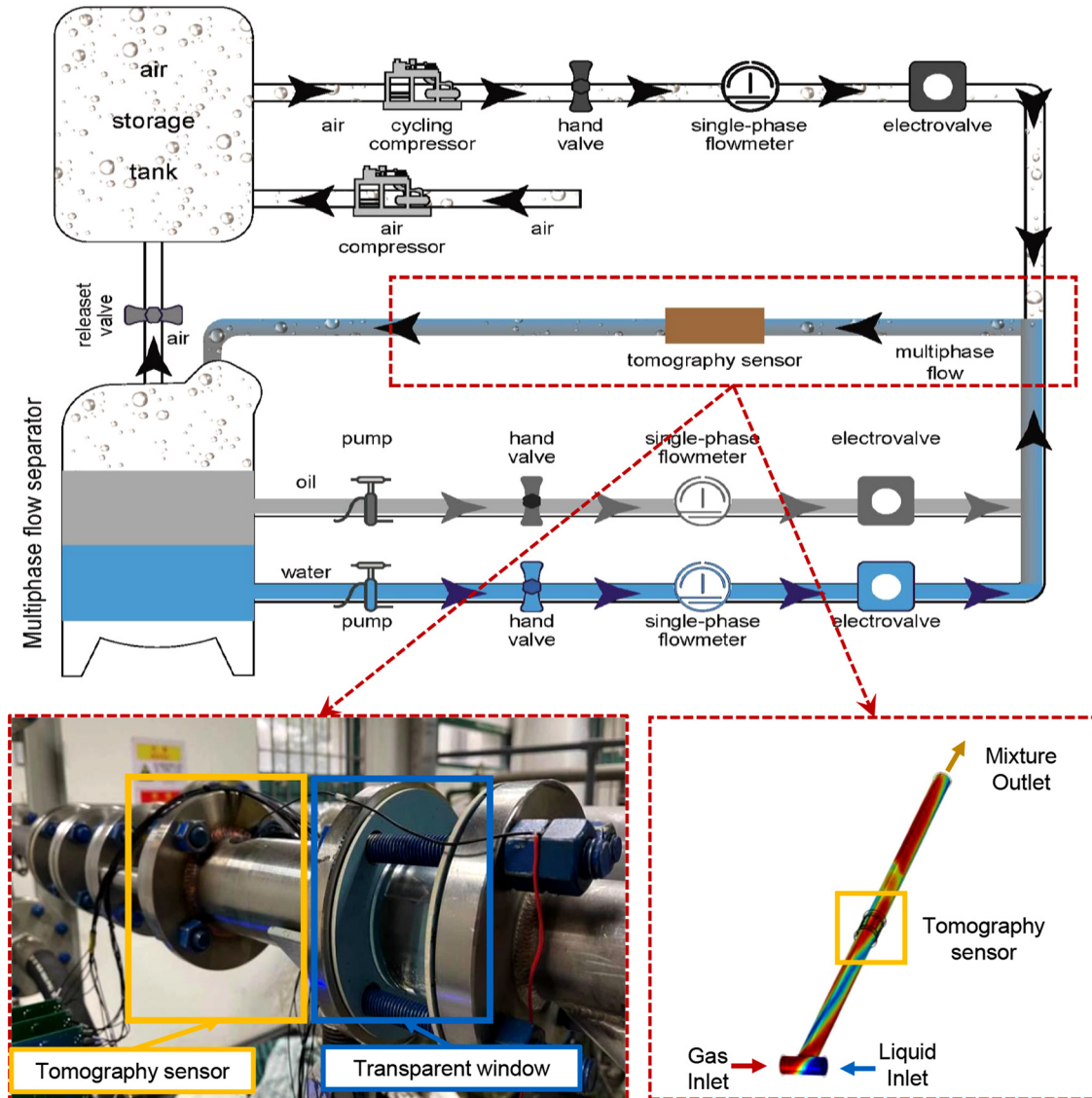


FIG. 1. The testing section of a pilot-scale multiphase flow testing facility.

owing to the breadth of the spatial scales of relevance, the discontinuous nature of the flows, the multitude of key driving parameters and the sensitivity to boundary conditions.<sup>40</sup> Compounding these limitations with the large noise-to-signal ratio of ET measurement makes the achievement of a close match between simulation and experiment a critical challenge.

## B. Simulation setup

For the majority of existing ET applications, EIT is commonly applied to visualize conductive flows such as water-dominated flows, while ECT is often used to image dielectric flows such as oil-dominated flows.<sup>9</sup> Therefore, two typical gas-liquid flows, i.e., the water-gas flow and the oil-gas flow, are virtually generated, and two coupling

simulations, i.e., the Water-gas flow field and Electric Currents field Coupling Simulation (WEC-CS) and the Oil-gas flow field and ElectroStatics field Coupling Simulation (OES-CS), are conducted to demonstrate the performance evaluation of EIT and ECT image reconstruction algorithms, respectively. Figures 4(a) and 4(b) show the virtual platform with a 16-electrode EIT sensor and a 12-electrode ECT sensor, respectively. The platform has two inlets, including a gas inlet, a liquid inlet, and a mixture outlet. By injecting gas and liquid into the system through the two inlets, gas-liquid two-phase flows are formed in the pipe and then flow out from the mixture outlet.

In WEC-CS, the gas-liquid flow generated by the fluid field is a water-gas flow, and the electric currents interface is applied to simulate the EIT sensor. For the water-gas flow, the densities of the water and gas are  $997$  and  $7.07 \text{ kg/m}^3$ , respectively. The dynamic viscosities

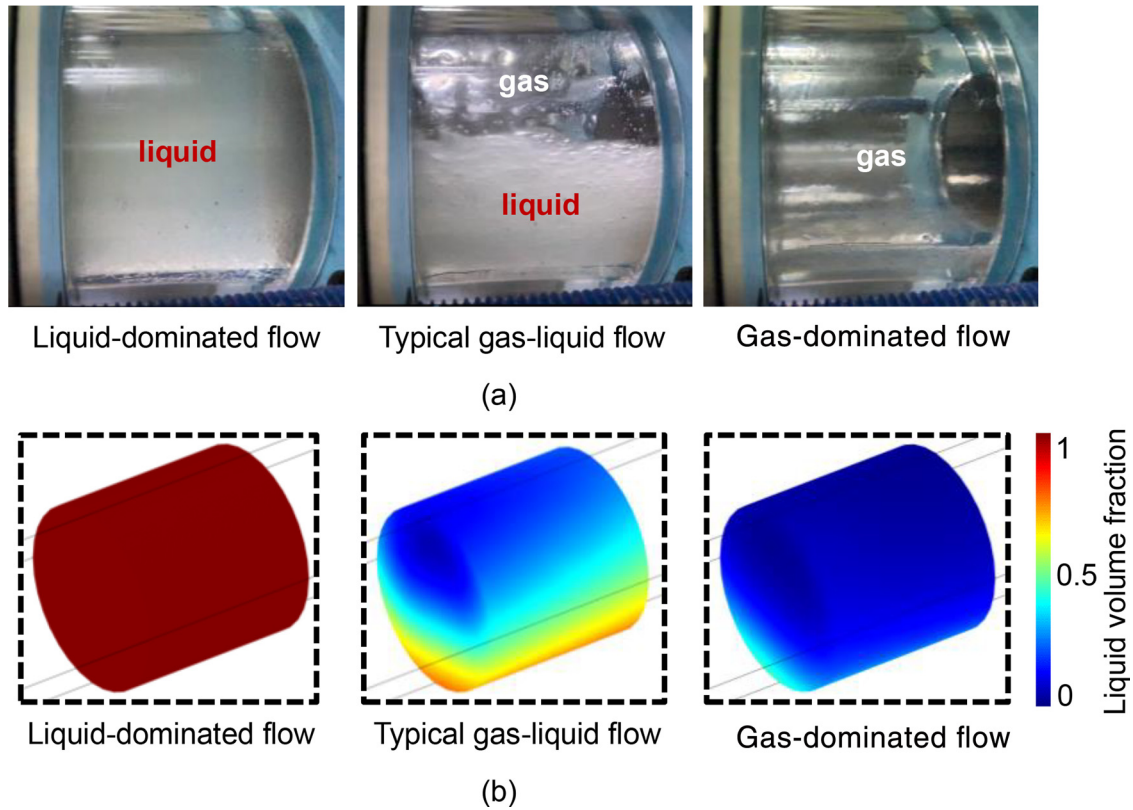


FIG. 2. Typical gas–liquid flows generated from (a) real flow facility and (b) 3D-FECM.

of the water and gas are  $1.01 \times 10^{-3}$  and  $1.81 \times 10^{-5}$  Pa s, respectively. For the electric currents interface, the electrical conductivity of pipe, electrode, air, and water is  $1 \times 10^{-14}$  S/m,  $7.41 \times 10^5$  S/m, 0 S/m, and 0.03 S/m, respectively. The relative permittivity of pipe, electrode, air, and water is 2.6, 1, 1, and 78, respectively. The equivalent conductivity

and permittivity of the mixing fluid are evaluated by Eqs. (8) and (9), respectively. Complementary alternating current pair with the value of  $[+1A, -1A]$  is alternately applied to the electrodes for induced boundary voltage measurement. A total of 4260129 tetrahedral elements, with a maximum element size of 2.73 mm and a minimum element size of 0.082 mm, were used to discretize the domain [see Fig. 5(a)]. The details of the WEC-CS setup are listed in Table I.

In OES-CS, the fluid field generates oil–gas flows, and the electrostatics interface is used to model the ECT sensor. For the oil–gas flow, the gas phase is air with a density of  $7.07 \text{ kg/m}^3$  and a dynamic viscosity of  $1.81 \times 10^{-5}$  Pa s. The liquid phase is white oil with a density of  $821 \text{ kg/m}^3$  and the dynamic viscosity of  $1.23 \times 10^{-2}$  Pa s. For the electrostatics interface, the relative permittivity of pipe and electrode is 2.6 and 1, respectively. The relative permittivity of oil and air is 2.18 and 1, respectively. The equivalent permittivity of the mixing fluid is evaluated by (9). We alternately injected the excitation voltage with the value of 1 V into the electrodes to measure the inter-electrode capacitances. Tetrahedral meshes consisting of 4104759 elements are generated, the maximum element size of the mesh is 3.5 mm and the minimum element size is 0.15 mm [see Fig. 5(b)]. The details of the OES-CS are listed in Table II.

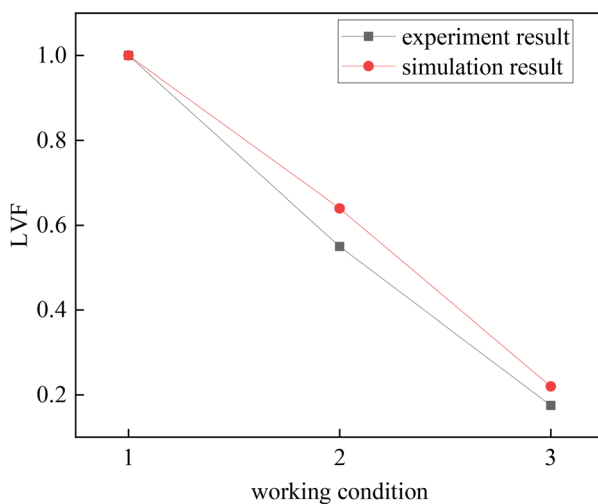


FIG. 3. Comparison of the simulation LVF with the experiment LVF.

### C. Coupling simulation results

Figures 6 and 7 show the WEC-CS and the OES-CS flowcharts, respectively. In coupling simulations, the gas–liquid flow data (i.e., the



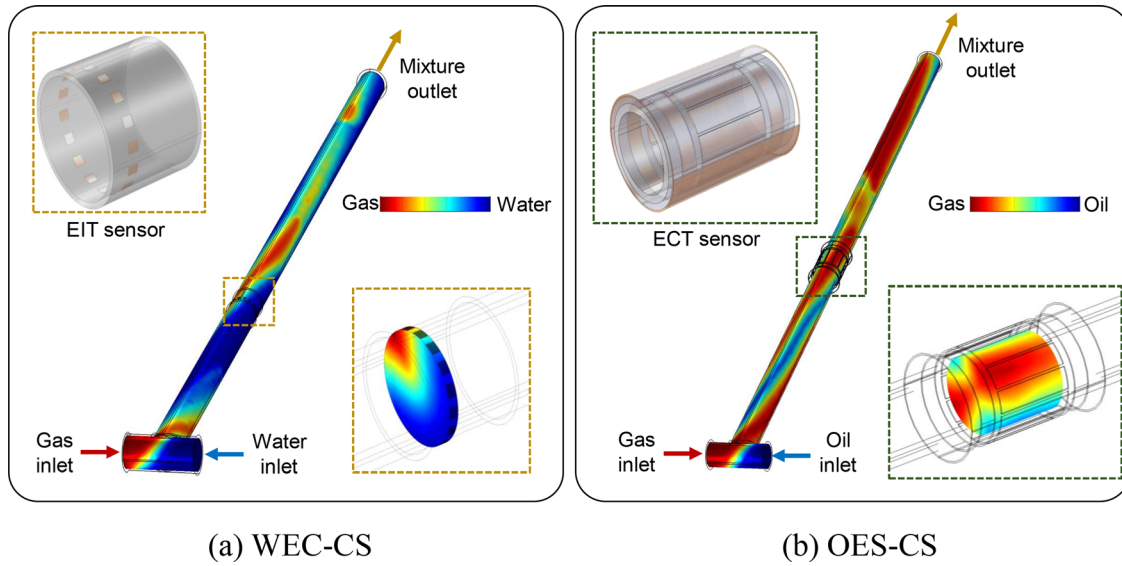


FIG. 4. Virtual multiphase flow measurement platform with ET sensors.

water–gas flow data and the oil–gas flow data) generated by the fluid field interfaces can be coupled to the electric field interfaces (i.e., the electric current field and the electrostatic field) to calculate the electric potential distribution within the virtual sensors. Through dynamic simulations following the EIT and ECT measurement principles, 104 induced boundary voltages, and 66 inter-electrode capacitances corresponding to the specific gas–liquid flows can be calculated and used for the image reconstructions of the water–gas and oil–gas flows in the DOI, respectively.

Figure 8 shows the representative sequential water–gas two-phase flows with the period range from 0 to 0.6 s generated by the fluid field interface in WEC-CS. The pipe is initially filled with water. With the gas and water injection, the water–gas two-phase flow is gradually formed and this mixture travels through the EIT sensor. Figure 8 also illustrates the derivation of the true distribution of conductivity variation in the EIT sensing region, which is adopted as the ground truth for quantitative comparison. The 3D fluid volumetric concentration distributions within the EIT sensor can be extracted from the time-varying water–gas two-phase flows and converted to 2D fluid volumetric concentration distribution by averaging voxel-to-voxel along the axial direction of the sensor. By setting the homogeneous water as the background reference (see case 1 in Fig. 8), the conductivity variation distributions can be obtained from the 2D fluid volumetric

concentration distributions. Through dynamic simulation following the EIT measurement principles, the relative change of induced boundary voltages corresponding to the specific water–gas flows in Fig. 8 can be calculated, as shown in Fig. 9. Previous research has shown that the induced boundary voltages have a nonlinear relationship with the water–gas flow in the sensing region of EIT, which can be used to reconstruct the conductivity distribution in the DOI.<sup>41,42</sup>

Typical sequential oil–gas two-phase flows generated by the fluid field interface during the OES-CS process are presented in Fig. 10. The pipe is initially filled with oil. With the oil and gas injection, oil–gas two-phase flows are formed in the pipe and flow through the ECT sensor. Like the derivation of the true distribution of conductivity variation, the true permittivity distribution can also be obtained from OES-CS and used as the ground truth for qualitative comparison. Through dynamic coupling simulation, the oil–gas flow data can be coupled to the ECT sensor to calculate inter-electrode capacitances. Figure 11 shows the calculated capacitances corresponding to the oil–gas two-phase flows in Fig. 10.

#### IV. QUANTITATIVE EVALUATION AND DISCUSSION

##### A. Case studies

We implemented three representative image reconstruction algorithms, i.e., the STR (one-step approach), IGLR (iterative approach),

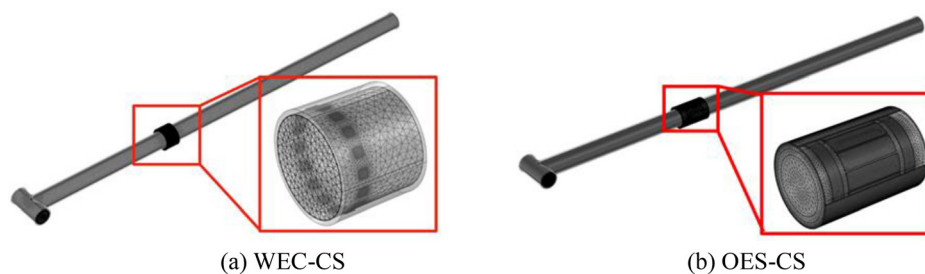


FIG. 5. Mesh of the 3D-FECM model.

TABLE I. WEC-CS setup.

Interface	Parameters	Value	Description
Fluid field interface	$\rho_w$ (kg/m <sup>3</sup> )	997	Density of water
	$\rho_g$ (kg/m <sup>3</sup> )	7.07	Density of gas
	$\mu_w$ (Pa·s)	$1.01 \times 10^{-3}$	Dynamic viscosity of water
	$\mu_g$ (Pa·s)	$1.81 \times 10^{-5}$	Dynamic viscosity of the gas
Electric currents interface	$\sigma_p$ (S/m)	$1 \times 10^{-14}$	Electrical conductivity of pipe
	$\sigma_e$ (S/m)	$7.41 \times 10^5$	Electrical conductivity of the electrode
	$\sigma_w$ (S/m)	0.03	Electrical conductivity of water
	$\sigma_g$ (S/m)	0	Electrical conductivity of the gas
	$\epsilon_p$	2.6	Relative permittivity of the pipe
	$\epsilon_e$	1	Relative permittivity of the electrode
	$\epsilon_w$	78	Relative permittivity of water
	$\epsilon_g$	1	Relative permittivity of gas
	$I$ (A)	+1, -1	Amplitude of excitation current

TABLE II. OES-CS setup.

Interface	Parameters	Value	Description
Fluid field interface	$\rho_o$ (kg/m <sup>3</sup> )	821	Density of oil
	$\rho_g$ (kg/m <sup>3</sup> )	7.07	Density of gas
	$\mu_o$ (Pa·s)	$1.23 \times 10^{-2}$	Dynamic viscosity of oil
Electrostatics interface	$\mu_g$ (Pa·s)	$1.81 \times 10^{-5}$	Dynamic viscosity of the gas
	$\epsilon_p$	2.6	Relative permittivity of the pipe
	$\epsilon_e$	1	Relative permittivity of the electrode
	$\epsilon_o$	2.18	Relative permittivity of oil
	$\epsilon_g$	1	Relative permittivity of gas
	$U$ (V)	1	Amplitude of excitation current

and SA-SBL (statistical approach), for EIT performance evaluation. The regularization coefficient  $\lambda$  for both STR and IGLR is determined using the L-curve method.<sup>43</sup> For IGLR, the images are reconstructed by adopting the optimal iteration number (i.e., the iteration with the

minimum relative image error) with the iteration step length of 0.008. For SA-SBL, the solution accuracy tolerance is set as 1E-7, the pattern relevance factor is fixed as 0.3, and the block size is selected as 4.

For ECT, two commonly used image reconstruction algorithms, i.e., the LBP and LI, are selected to reconstruct the cross-sectional permittivity distribution. To evaluate the best performance of the LI, the optimal iteration number with a relaxation factor of 1 is adopted. We also introduce the TR-GL in ECT image reconstruction for comparison and adopt the L-curve method to determine the regularization coefficient.

To simulate the background noise of the real-world ET system and evaluate the noise performance of the selected algorithms, we add the additive noise with different SNR levels, i.e., 80, 70, 60, 50, 40, 30, and 20 dB to the virtual ET measurements for image reconstruction. To quantitatively evaluate the quality of reconstructed images, two standard metrics, i.e., Relative Image Error (RIE)<sup>35</sup> and Structural Similarity Index Measure (SSIM),<sup>44</sup> are adopted,

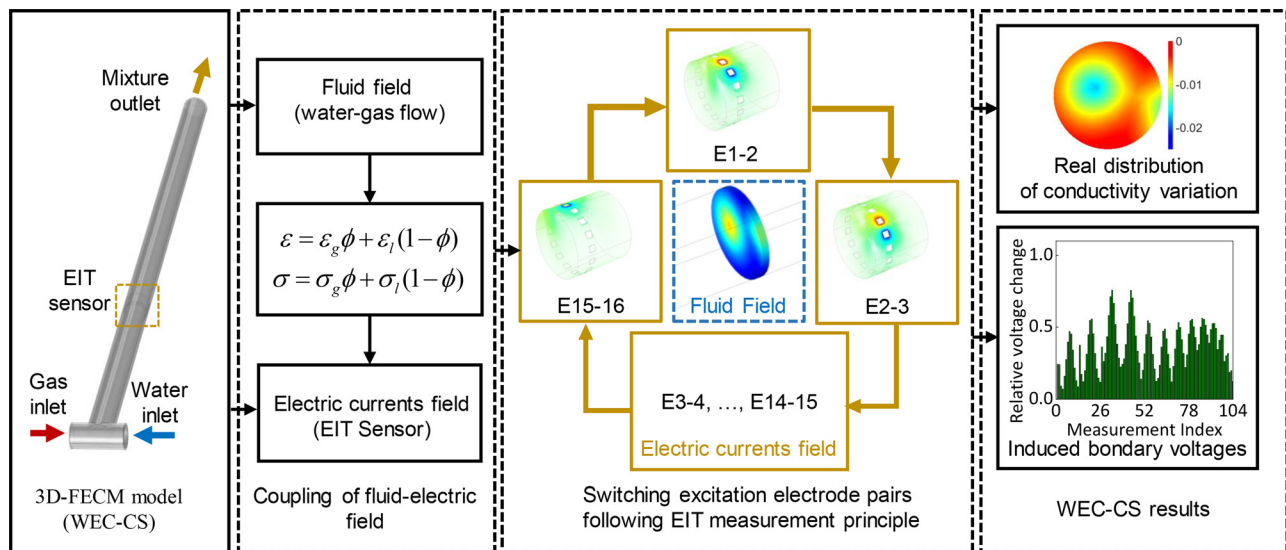


FIG. 6. Flowchart of WEC-CS.

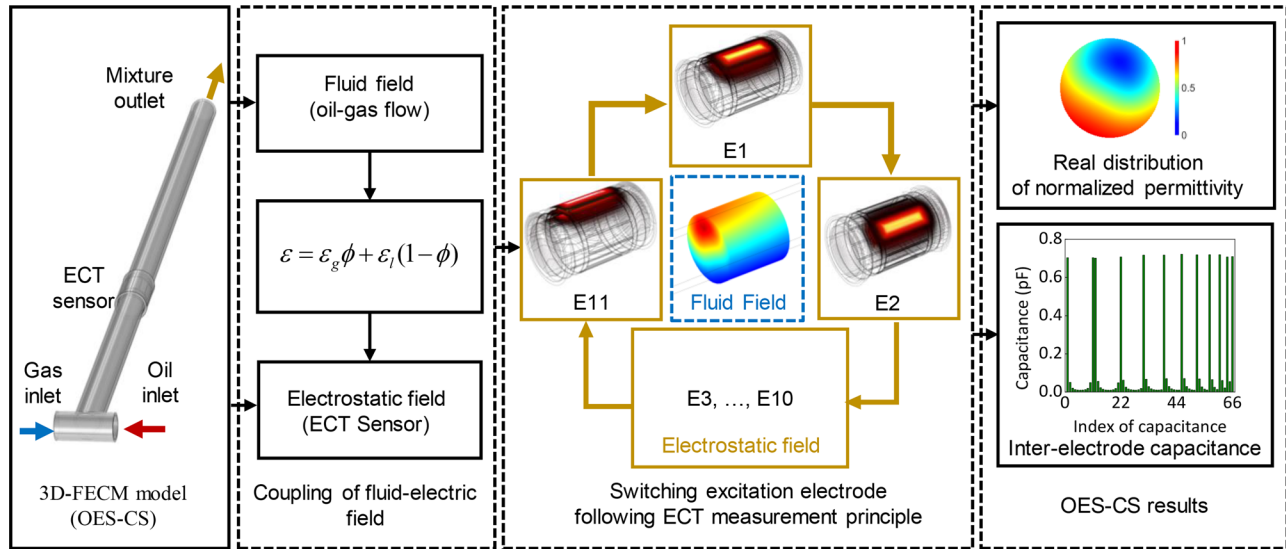


FIG. 7. Flowchart of OES-CS.

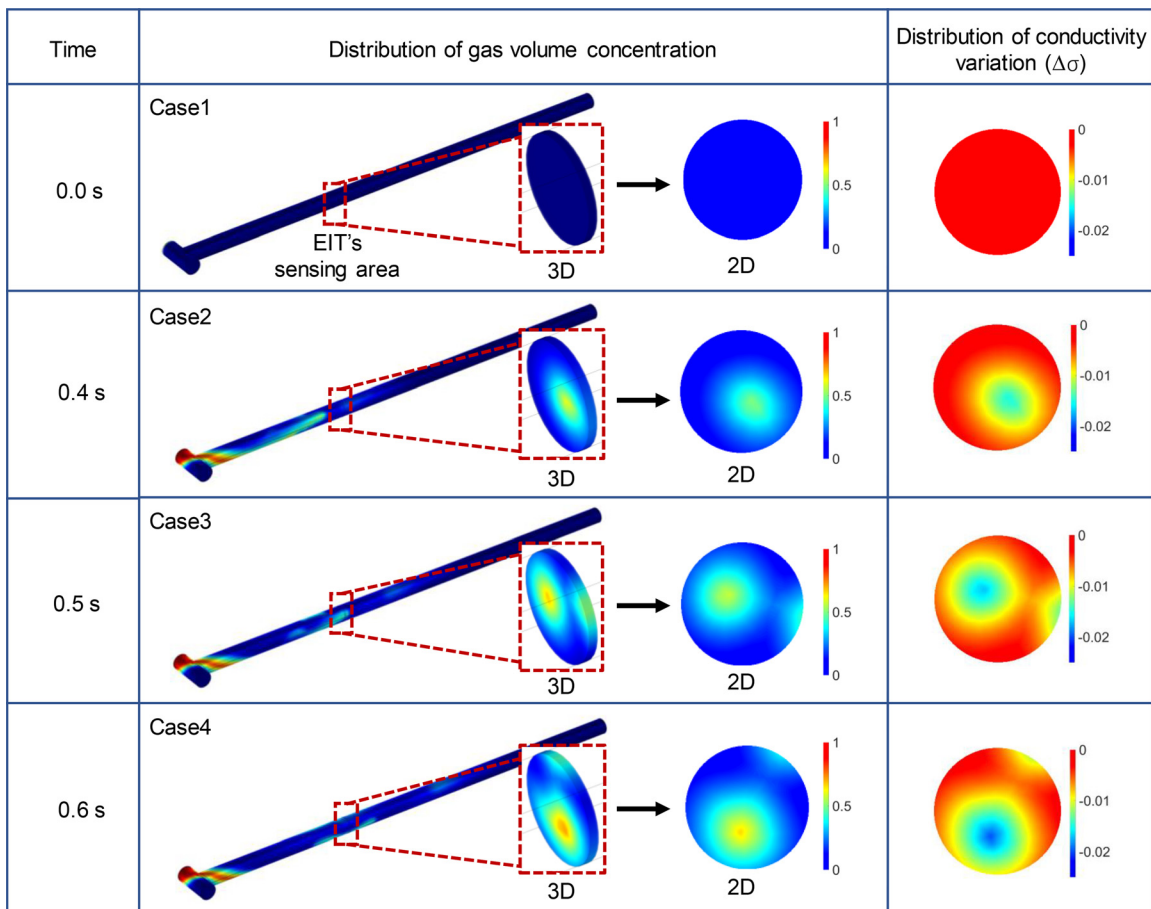


FIG. 8. A representative set of sequential water–gas flows obtained from WEC-CS.

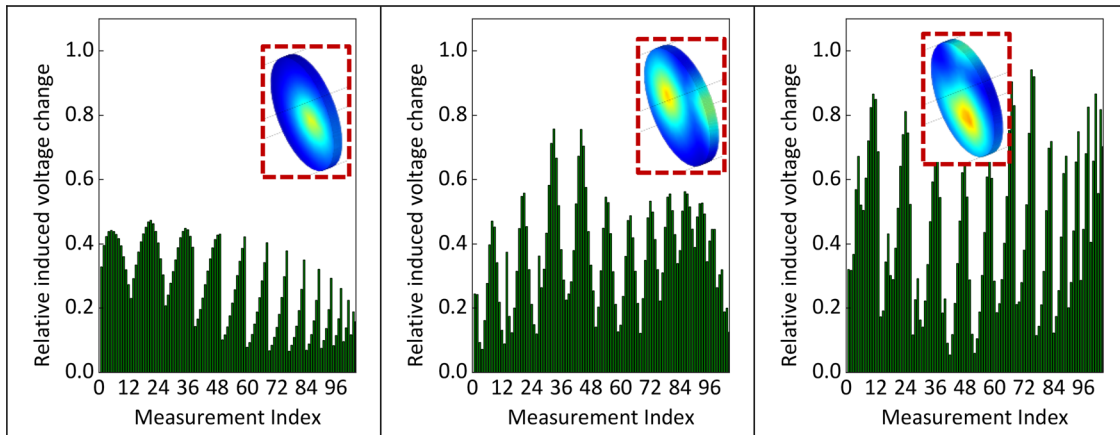


FIG. 9. Relative changes of induced boundary voltages obtained from WEC-CS.

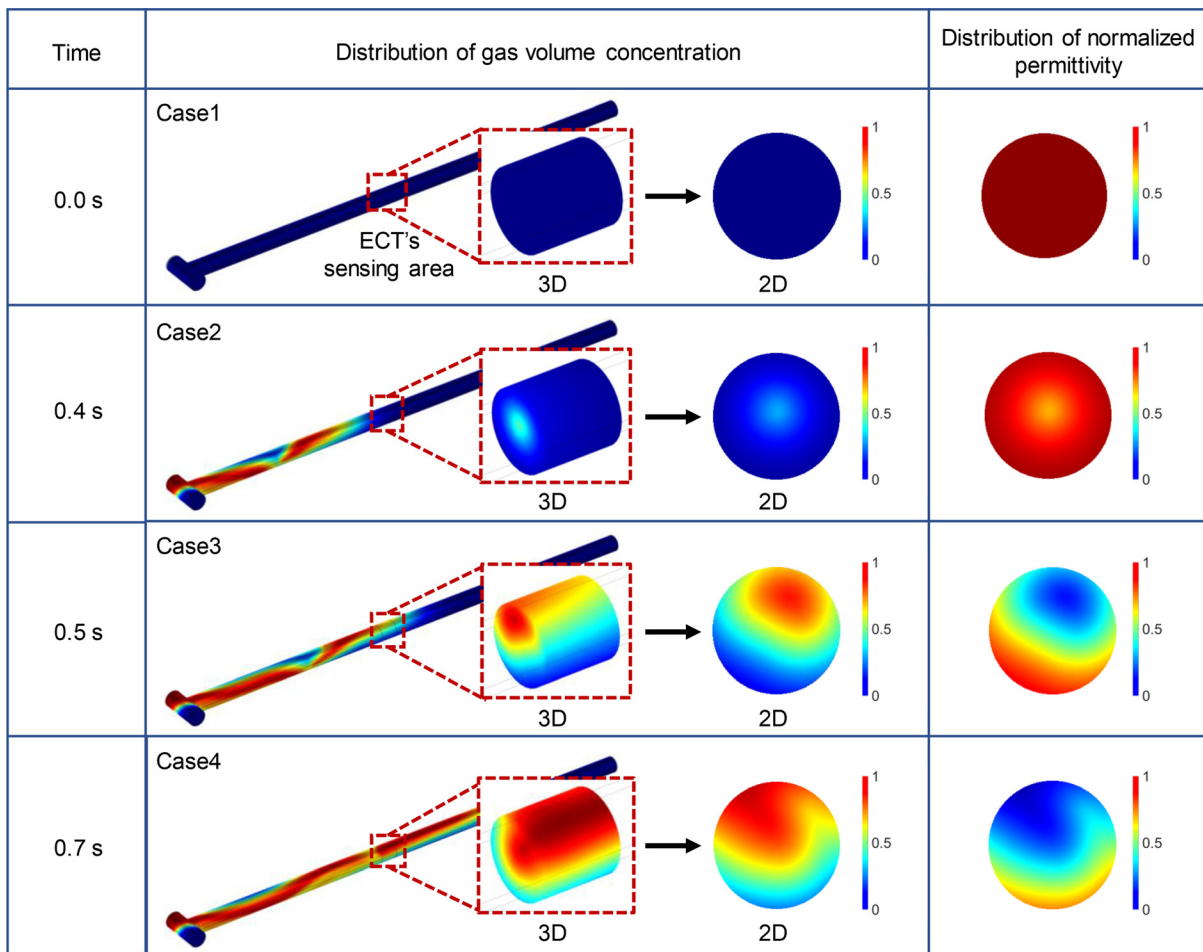


FIG. 10. A representative set of sequential oil-gas flows obtained from OES-CS.

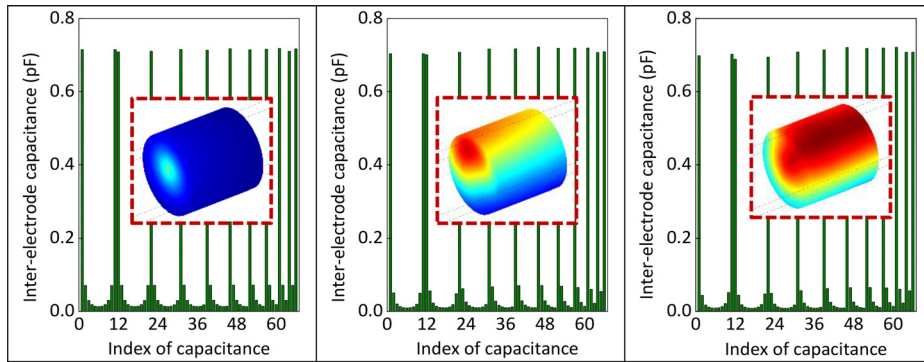
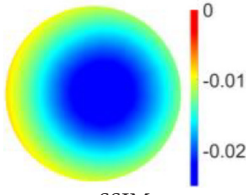
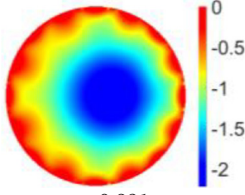
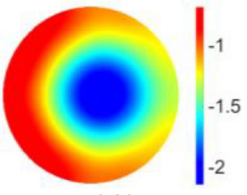
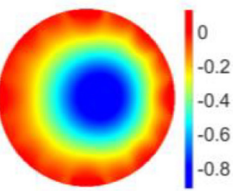


FIG. 11. Inter-electrode capacitances obtained from OES-CS.

TABLE III. EIT image reconstruction results based on noise-contaminated data with 60 dB SNR.

Phantom	Ground truth	Reconstructed images		
		STR	IGLR	SA-SBL
P1				
	SSIM RIE	0.842 0.145	0.842 0.145	0.842 0.145
P2				
	SSIM RIE	0.829 0.194	0.953 0.069	0.856 0.145
P3				
	SSIM RIE	0.784 0.144	0.942 0.082	0.883 0.157
P4				
	SSIM RIE	0.849 0.136	0.934 0.086	0.949 0.148

TABLE III. (Continued.)

Phantom	Ground truth	Reconstructed images		
		STR	IGLR	SA-SBL
P5				
	SSIM RIE	0.891 0.107	0.905 0.143	0.926 0.124

$$RIE = \frac{\|\theta - \zeta\|_2}{\|\zeta\|_2}, \tag{22}$$

$$SSIM = \frac{(2\psi_\theta\psi_\zeta + M_1)(2\eta_{\theta\zeta} + M_2)}{(\psi_\theta^2 + \psi_\zeta^2 + M_1)(\eta_\theta^2 + \eta_\zeta^2 + M_2)}, \tag{23}$$

where  $\theta$  represents the reconstructed image,  $\zeta$  represents the actual image,  $\psi_\theta$  and  $\psi_\zeta$  are the mean intensities of  $\theta$  and  $\zeta$ , respectively,  $\eta_\theta$  and  $\eta_\zeta$  are the variances of  $\theta$  and  $\zeta$ , respectively,  $\eta_{\theta\zeta}$  is the cross-covariance for  $\theta$  and  $\zeta$ , and  $M_1$  and  $M_2$  are constants.

**B. Evaluation results and discussion**

**1. Electrical impedance tomography**

Table III displays the reconstructed EIT images and corresponding quantitative evaluations (i.e., the SSIM and the RIE) based on STR, IGLR, and SA-SBL for five selected phantoms (i.e., P1, P2, P3, P4, and P5). These results adopt noise-contaminated voltage data with 60 dB SNR for image reconstruction. For the given phantoms, the reconstructed images of all the selected algorithms have similar conductivity variations with the ground truth. Compared to IGLR and SA-SBL, the reconstructed images

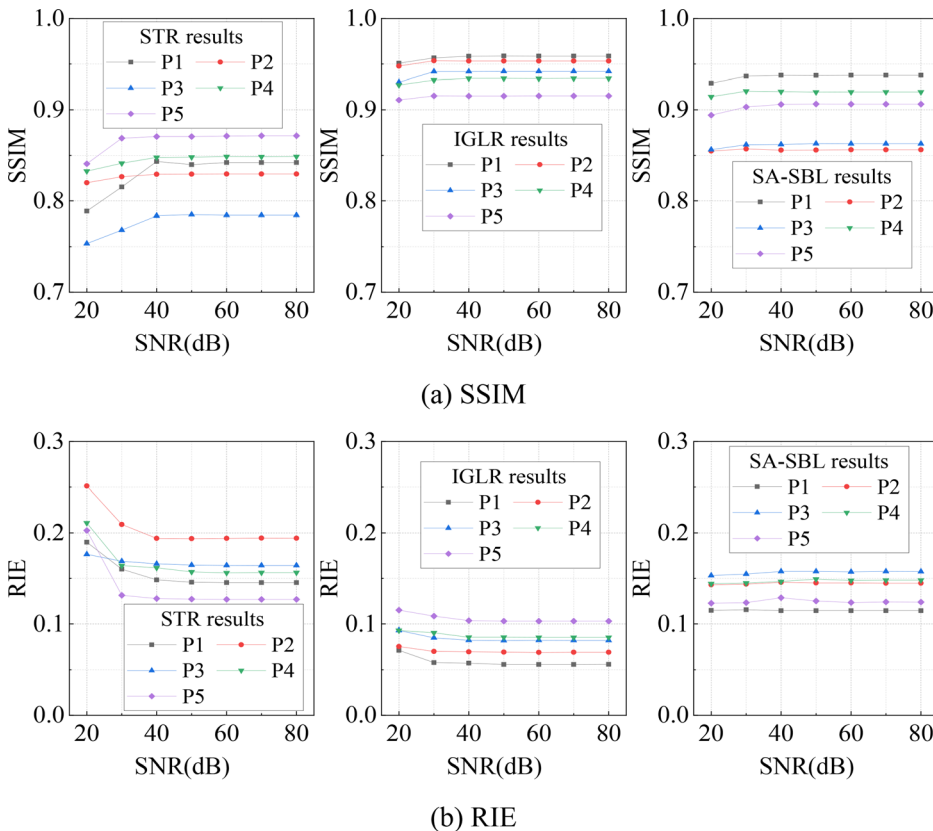
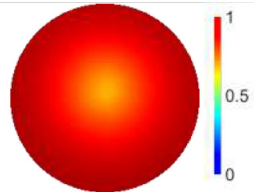
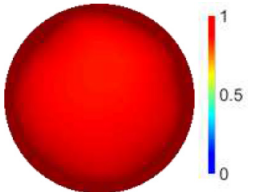
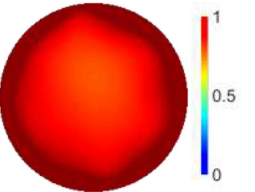
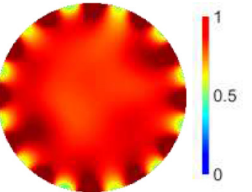
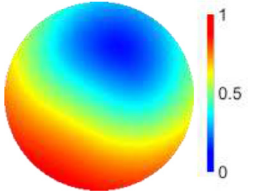
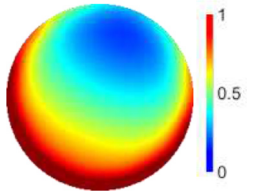
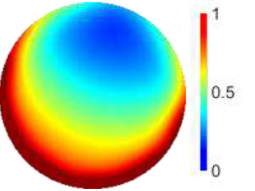
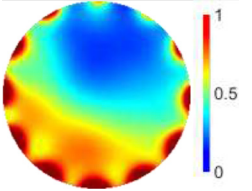
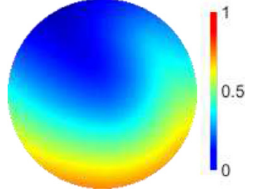
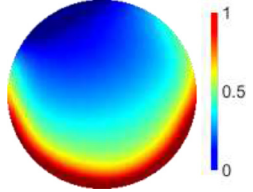
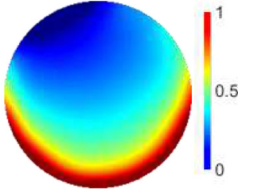
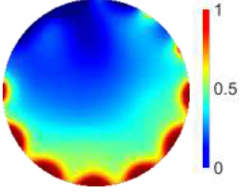
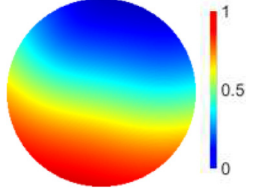
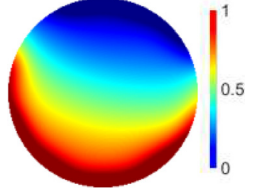
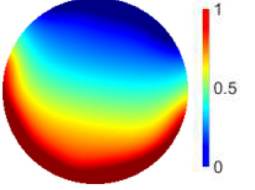
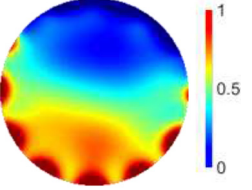
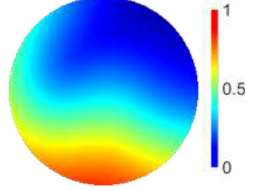
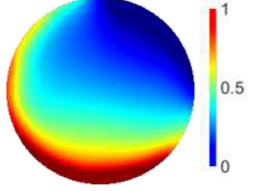
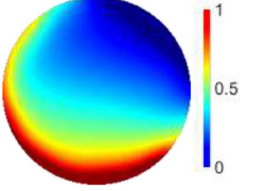
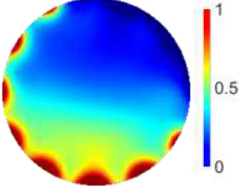


FIG. 12. Quantitative evaluation results of EIT images reconstructed by STR, IGLR, and SA-SBL.

TABLE IV. ECT image reconstruction results based on noise-contaminated data with 60 dB SNR.

Phantom	Ground truth	Reconstructed images		
		LBP	LI	TR-GL
P1	 SSIM RIE	 0.987 0.044	 0.987 0.038	 0.731 0.116
P2	 SSIM RIE	 0.925 0.180	 0.926 0.178	 0.780 0.167
P3	 SSIM RIE	 0.825 0.290	 0.829 0.286	 0.731 0.235
P4	 SSIM RIE	 0.827 0.156	 0.833 0.151	 0.709 0.156
P5	 SSIM RIE	 0.800 0.247	 0.813 0.245	 0.741 0.223

using STR show more substantial artifacts and graver distortion. The relevant quantitative evaluation results further confirm the worst results of STR as it yields the largest RIE, i.e., 0.194, and the lowest SSIM, i.e., 0.784. As for the results of IGLR and SA-SBL, image qualities are improved with fewer artifacts and distortion. The reconstructed images using IGLR have

a higher SSIM (above 0.905) and smaller RIE (below 0.143), indicating the superior reconstruction imaging quality of IGLR with more accurate conductivity estimations of the flows.

The performance of the three selected algorithms is further validated on noise-contaminated voltage data with different SNR levels

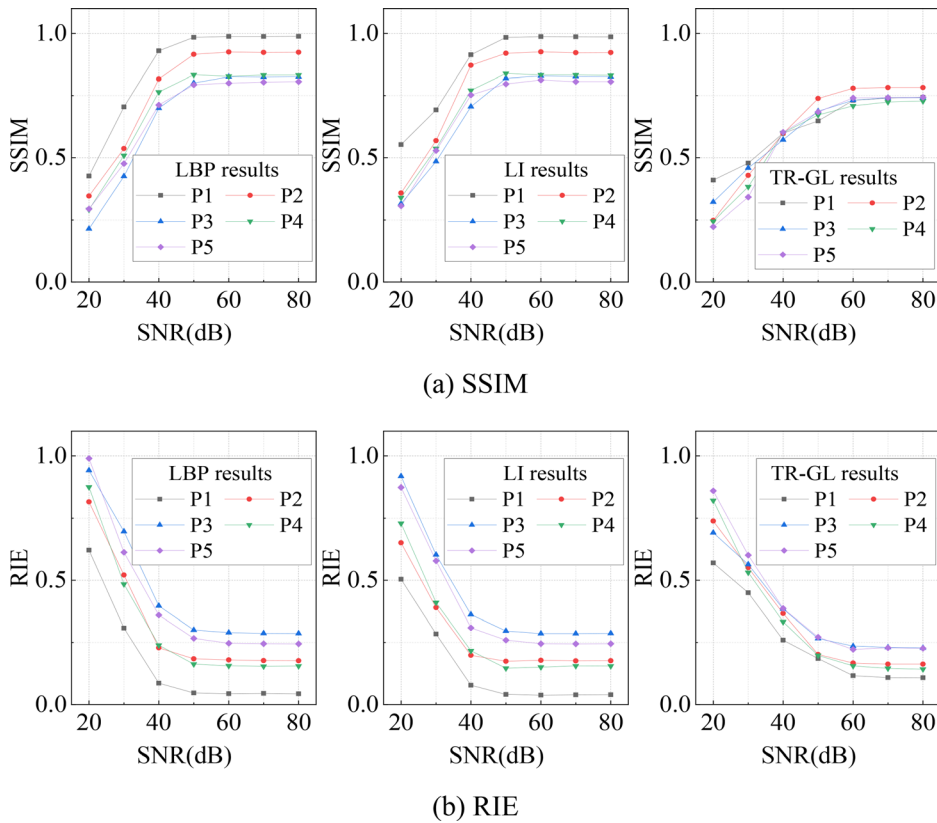


FIG. 13. Quantitative evaluation results of ECT images reconstructed by LBP, LI, and TR-GL.

ranging from 20 to 80 dB, and the corresponding comparison results in terms of SSIM and RIE are presented in Fig. 12. The comparison results further demonstrate that the IGLR achieves the best reconstruction imaging quality among these selected algorithms, as the SSIM of the IGLR result is within 0.90 to 0.95, and its RIE changes from 0.2 to 0.1 for the SNRs ranging from 20 to 80 dB, which are better than those of the STR result (i.e., SSIM: from 0.90 to 0.95; RIE: from 0.1 to 0.2) and the SA-SBL result (i.e., SSIM: from 0.90 to 0.95; RIE: from 0.1 to 0.2). We also observe that the SSIMs increase, and RIEs decrease with the increase in SNR from 20 to 40 dB for all the results. After that, the SSIMs and the RIEs remain nearly unchanged as SNR continues to rise, indicating that the noise with SNR above 40 dB has no noticeable effect on the image reconstruction performance of the given algorithms. It is worth noting that the RIE of the SA-SBL result increases by only 0.1 when the SNR decreases from 80 to 20 dB, much less than those of the IGLR results (rise by 0.2) and the STR results (rise by 0.3). Overall, SA-SBL presents excellent noise reduction performance.

## 2. Electrical capacitance tomography

Table IV compares the ECT image reconstruction results using different algorithms, i.e., LBP, LI, and TR-GL. For the given phantoms, all the reconstructed images using LBP are similar to those using LI, and the values of SSIM and RIE are also close to those from LI, indicating that the LBP and the LI demonstrate similar performance in permittivity distribution reconstruction in multiphase flow imaging. In comparison, the reconstructed images using TR-GL present more

vital distortion and show more severe deterioration in the boundary area of the pipe, with the value of the SSIM for each phantom being 0.731, 0.780, 0.731, 0.709, and 0.741, much lower than those of the LBP results (0.987, 0.925, 0.825, 0.832, and 0.806) and the LI results (0.987, 0.926, 0.829, 0.833, and 0.813).

Figure 13 presents the quantitative evaluations of the ECT image reconstruction results regarding SSIM and RIE concerning different SNR levels. For all the given algorithms and phantoms, the SSIMs increase and the RIEs decrease as the SNRs increase from 20 dB to 60 dB, and then both SSIMs and RIEs tend to stabilize with the further increasing SNR. This indicates that the noise with SNR higher than or equal to 60 dB has no noticeable effect on the performance of these selected algorithms. However, the noise with SNR lower than 50 dB dramatically reduces the image reconstruction quality.

## V. CONCLUSION

This study proposed a virtual platform for quantitative multiphase flow imaging performance evaluation using electrical tomography. The virtual platform is centered on a three-dimensional Fluid-Electric field Coupling model (3D-FECM) based on which the Water-gas flow field and Electric Currents field Coupling Simulation (WEC-CS) and the Oil-gas flow field and ElectroStatics field Coupling Simulation (OES-CS) are separately implemented for imaging performance evaluation of EIT and ECT. As case studies, three representative image reconstruction algorithms of EIT were assessed on our virtual platform. The SA-SBL presented the best noise reduction performance among other algorithms from the comparison. We also selected three



prevailing ECT image reconstruction algorithms for quantitative performance evaluation of ECT in multiphase flow imaging. The results showed that, for the given cases, the LBP and the LI demonstrate similar performance for oil–gas flow imaging, while the image reconstructed by TR-GL presents more substantial distortion. The noise with SNR lower than 50 dB had a significant influence on the image quality of these three selected algorithms.

The proposed virtual platform could model the dynamic behavior of the real multiphase flows, making it a more persuasive assessment approach compared with static simulation and phantom-based experimental methods. Moreover, by conducting dynamic coupling simulations, instantaneous ET and real images can be obtained simultaneously, creating favorable conditions for parameter optimization of model-based ET image reconstruction algorithms and the generation of closer-to-reality datasets for training learning-based algorithms in multiphase flow imaging.

While the underlying coupled numerical model employed in this work does not aim to investigate specific flow patterns, it unlocks a robust and accurate approach to mapping permittivity/conductivity signal into phase distribution, thus enabling a much-needed yet unsolved method to extract real-time multiphase flow features. This work offers as rigorous as possible a characterization of the capability to reconstruct complex dynamic flow mixtures, paving the way for accurate flow physics research and applications in multiphase flows.

## ACKNOWLEDGMENTS

This work was supported by the European Union's Horizon 2020 research and innovation programme under the Marie Skłodowska-Curie grant agreement (Grant No. 801215) and the University of Edinburgh Data-Driven Innovation programme, part of the Edinburgh and South East Scotland City Region Deal, Data Driven Innovation Chancellor's Fellowship, and National Natural Science Foundation of China (Grant No. 51906209).

## AUTHOR DECLARATIONS

### Conflict of Interest

The authors have no conflicts to disclose.

### Author Contributions

**Shengnan Wang:** Data curation (equal); Funding acquisition (equal); Investigation (equal); Methodology (equal); Writing – original draft (equal). **Francesco Giorgio-Serchi:** Formal analysis (supporting); Validation (supporting); Writing – review & editing (supporting). **Yunjie Yang:** Funding acquisition (equal); Methodology (equal); Supervision (equal); Writing – review & editing (equal).

## DATA AVAILABILITY

The data that support the findings of this study are available from the corresponding author upon reasonable request.

## REFERENCES

- <sup>1</sup>W. Deabes, A. E. Abdel-Hakim, K. E. Bouazza, and H. Althobaiti, "Adversarial resolution enhancement for electrical capacitance tomography image reconstruction," *Sensors* **22**, 3142 (2022).
- <sup>2</sup>O. T. Kajero, M. Abdulkadir, L. Abdulkareem, and B. J. Azzopardi, "Experimental study of viscous effects on flow pattern and bubble behavior in a small diameter bubble column," *Phys. Fluids* **30**, 093101 (2018).
- <sup>3</sup>W. Q. Yang and L. H. Peng, "Image reconstruction algorithms for electrical capacitance tomography," *Meas. Sci. Technol.* **14**, R1 (2003).
- <sup>4</sup>J. V. Jimenez, A. J. Weirauch, C. A. Culter, P. J. Choi, and R. C. Hyzy, "Electrical impedance tomography in acute respiratory distress syndrome management," *Crit. Care Med.* **50**, 1210 (2022).
- <sup>5</sup>J. E. Butler and R. T. Bonnecaze, "Imaging of particle shear migration with electrical impedance tomography," *Phys. Fluids* **11**, 1982 (1999).
- <sup>6</sup>O. A. Brabant, D. P. Byrne, M. Sacks, F. M. Martinez, A. L. Rasis, J. B. Araos, A. D. Waldmann, J. P. Schramel, A. Ambrosio, G. Hosgood, C. Braun, U. Auer, U. Bleul, N. Herteman, C. J. Secombe, A. Schoster, J. Soares, S. Beazley, C. Meira, A. Adler, and M. Mosing, "Thoracic electrical impedance tomography—The 2022 Veterinary Consensus Statement," *Front. Vet. Sci.* **9**, 946911 (2022).
- <sup>7</sup>R. K. Rasel, S. M. Chowdhury, Q. M. Marashdeh, and F. L. Teixeira, "Review of selected advances in electrical capacitance volume tomography for multiphase flow monitoring," *Energies* **15**, 5285 (2022).
- <sup>8</sup>R. L. Powell, "Experimental techniques for multiphase flows," *Phys. Fluids* **20**, 040605 (2008).
- <sup>9</sup>J. F. Yao and M. Takei, "Application of process tomography to multiphase flow measurement in industrial and biomedical fields: A review," *IEEE Sens. J.* **17**, 8196 (2017).
- <sup>10</sup>D. Wanta, O. Makowiecka, W. T. Smolik, J. Kryszyn, G. Domanski, M. Midura, and P. Wroblewski, "Numerical evaluation of complex capacitance measurement using pulse excitation in electrical capacitance tomography," *Electronics* **11**, 1864 (2022).
- <sup>11</sup>R. Basak and K. A. Wahid, "A rapid, low-cost, and high-precision multifrequency electrical impedance tomography data acquisition system for plant phenotyping," *Remote Sens.* **14**, 3214 (2022).
- <sup>12</sup>M. G. Rasteiro, R. Silva, F. A. P. Garcia, and P. Faia, "Electrical tomography: A review of configurations and applications to particulate processes," *Kona Powder Part. J.* **29**, 67 (2011).
- <sup>13</sup>F. A. E. Revelo, V. H. M. Leyton, and C. F. R. Rodas, "Electrical impedance tomography: Hardware fundamentals and medical applications," *Ing. Solidaria* **16**(3), (2020).
- <sup>14</sup>E. Alruwaili and J. Li, "Majorization-minimization total variation solution methods for electrical impedance tomography," *Mathematics* **10**, 1469 (2022).
- <sup>15</sup>S. C. Zhong, Y. B. Wang, Y. K. Zheng, S. J. Wu, X. Chang, and W. Zhu, "Electrical resistivity tomography with smooth sparse regularization," *Geophys. Prospect.* **69**, 1773 (2021).
- <sup>16</sup>J. M. Ye, H. G. Wang, and W. Q. Yang, "Image reconstruction for electrical capacitance tomography based on sparse representation," *IEEE Trans. Instrum. Meas.* **64**, 89 (2015).
- <sup>17</sup>Y. A. Wahab, R. A. Rahim, M. H. F. Rahiman, S. R. Aw, F. R. M. Yunus, J. Puspanathan, N. M. N. Ayob, L. P. Ling, H. A. Rahim, I. L. Ahmad, A. Jonet, C. K. Seng, and T. K. Sek, "Inverse problem: comparison between linear back-projection algorithm and filtered back-projection algorithm in soft-field tomography," *Int. J. Integrated Eng.* **9**, 32 (2017).
- <sup>18</sup>Z. Xu, J. C. Huang, Y. D. Jiang, B. L. Wang, Z. Y. Huang, and M. Soleimani, "An image reconstruction algorithm for a 12-electrode capacitively coupled electrical resistance tomography system under 2-electrode excitation strategy," *IEEE Trans. Instrum. Meas.* **70**, 4505911 (2021).
- <sup>19</sup>S. J. Hamilton, R. B. Lionheart, and A. Adler, "Comparing D-bar and common regularization-based methods for electrical impedance tomography," *Physiol. Meas.* **40**, 044004 (2019).
- <sup>20</sup>S. H. Liu, J. B. Jia, Y. M. D. Zhang, and Y. J. Yang, "Image reconstruction in electrical impedance tomography based on structure-aware sparse Bayesian learning," *IEEE Trans. Med. Imaging* **37**, 2090 (2018).
- <sup>21</sup>Y. J. Yang and J. B. Jia, "An image reconstruction algorithm for electrical impedance tomography using adaptive group sparsity constraint," *IEEE Trans. Instrum. Meas.* **66**, 2295 (2017).
- <sup>22</sup>W. Herzberg, D. B. Rowe, A. Hauptmann, and S. J. Hamilton, "Graph convolutional networks for model-based learning in nonlinear inverse problems," *IEEE Trans. Comput. Imaging* **7**, 1341 (2021).

- <sup>23</sup>L. Q. Cui, P. Tian, C. Wang, B. Jia, Y. X. Wang, L. Qin, X. Deng, L. Zhang, and J. M. Qin, "Iterative weighted fidelity and hybrid regularization-based algorithm for ECT," *Meas. Sci. Technol.* **33**, 065404 (2022).
- <sup>24</sup>M. S. Hossain, M. T. Abir, M. S. Alam, J. L. Volakis, and M. A. Islam, "An algorithm to image individual phase fractions of multiphase flows using electrical capacitance tomography," *IEEE Sens. J.* **20**, 14924 (2020).
- <sup>25</sup>J. M. Ye, W. Q. Yang, and C. Wang, "Investigation of spatial resolution of electrical capacitance tomography based on coupling simulation," *IEEE Trans. Instrum. Meas.* **69**, 8919 (2020).
- <sup>26</sup>J. Puspanathan, R. A. Rahim, F. A. Phang, E. J. Mohamad, N. M. N. Ayob, M. H. F. Rahiman, and C. K. Seong, "Single-plane dual-modality tomography for multiphase flow imaging by integrating electrical capacitance and ultrasonic sensors," *IEEE Sens. J.* **17**, 6368 (2017).
- <sup>27</sup>Y. Mamatjan, B. Grychtol, P. Gaggero, J. Justiz, V. M. Koch, and A. Adler, "Evaluation and real-time monitoring of data quality in electrical impedance tomography," *IEEE Trans. Med. Imaging* **32**, 1997 (2013).
- <sup>28</sup>Y. Wu, D. Jiang, R. Yerworth, and A. Demosthenous, "An imaged based method for universal performance evaluation of electrical impedance tomography systems," *IEEE Trans. Biomed. Circuits Syst.* **15**, 464 (2021).
- <sup>29</sup>J. M. Ye, H. G. Wang, Y. Li, and W. Q. Yang, "Coupling of fluid field and electrostatic field for electrical capacitance tomography," *IEEE Trans. Instrum. Meas.* **64**, 3334 (2015).
- <sup>30</sup>S. N. Wang, J. M. Ye, and Y. J. Yang, "Quantitative measurement of two-phase flow by electrical capacitance tomography based on 3D coupling field simulation," *IEEE Sens. J.* **21**, 20136 (2021).
- <sup>31</sup>D. L. Brown, R. Cortez, and M. L. Minion, "Accurate projection methods for the incompressible Navier-Stokes equations," *J. Comput. Phys.* **168**, 464 (2001).
- <sup>32</sup>E. Olsson and G. Kreiss, "A conservative level set method for two phase flow," *J. Comput. Phys.* **210**, 225 (2005).
- <sup>33</sup>Y. A. Wahab, R. A. Rahim, M. H. F. Rahiman, L. P. Ling, A. W. S. Ridzuan, F. R. M. Yunus, H. A. Rahim, H. Wahid, S. Sahlan, M. A. M. Yunus, N. A. Wahab, and A. A. A. Ahmad, "Compatible study on utilizing frequency for non-invasive electrical resistance tomography using COMSOL multiphysics," *J. Teknol.* **73**, 65–70 (2015).
- <sup>34</sup>Z. Y. Che and K. L. Collins, "An upper bound on Wiener Indices of maximal planar graphs," *Discrete Appl. Math.* **258**, 76 (2019).
- <sup>35</sup>Z. Liu and Y. J. Yang, "Multimodal image reconstruction of electrical impedance tomography using Kernel method," *IEEE Trans. Instrum. Meas.* **71**, 5002012 (2022).
- <sup>36</sup>M. Vauhkonen, D. Vadasz, P. A. Karjalainen, E. Somersalo, and J. P. Kaipio, "Tikhonov regularization and prior information in electrical impedance tomography," *IEEE Trans. Med. Imaging* **17**, 285 (1998).
- <sup>37</sup>Y. J. Yang, J. B. Jia, N. Polydorides, and H. McCann, "Effect of structured packing on EIT image reconstruction," in *IEEE International Conference on Imaging Systems and Techniques (IST) Proceedings* (IEEE, Santorini, Greece, 2014).
- <sup>38</sup>S. N. Wang, J. Li, M. Kong, C. L. Xu, and S. M. Wang, "Electrostatic effect on AC-based ECT and its elimination," *IEEE Sens. J.* **17**, 8081 (2017).
- <sup>39</sup>S. Z. Islami rad, R. Gholipour Peyvandi, and S. Sadzadeh, "Determination of the volume fraction in (water-gas-oil-air) multiphase flows using a simple and low-cost technique: Artificial neural networks," *Phys. Fluids* **31**, 093301 (2019).
- <sup>40</sup>S. Subramaniam, "Multiphase flows: Rich physics, challenging theory, and big simulations," *Phys. Rev. Fluids* **5**, 110520 (2020).
- <sup>41</sup>S. P. Pellegrini, F. C. Trigo, and R. G. Lima, "Adaptive Kalman filter-based information fusion in electrical impedance tomography for a two-phase flow," *Mech. Syst. Signal Process.* **150**, 107326 (2021).
- <sup>42</sup>J. Polansky and M. Wang, "Proper orthogonal decomposition as a technique for identifying two-phase flow pattern based on electrical impedance tomography," *Flow Meas. Instrum.* **53**, 126 (2017).
- <sup>43</sup>J. Wagner, S. Gschossmann, and M. Schagerl, "On the capability of measuring actual strain values with electrical impedance tomography using planar silk-screen printed elastoresistive sensors," *IEEE Sens. J.* **21**, 5798 (2021).
- <sup>44</sup>M. P. Sampat, Z. Wang, S. Gupta, A. C. Bovik, and M. K. Markey, "Complex wavelet structural similarity: A new image similarity index," *IEEE Trans. Image Process.* **18**, 2385 (2009).